


# Imaging an Acoustic Topological Edge Mode on a Patterned Substrate with Microwave Impedance Microscopy

Y. Nii<sup>1,2,\*</sup> and Y. Onose<sup>1</sup>

<sup>1</sup>*Institute for Materials Research, Tohoku University, Sendai 980-8577, Japan*

<sup>2</sup>*PRESTO, Japan Science and Technology Agency (JST), Kawaguchi 332-0012, Japan*

 (Received 4 June 2022; revised 9 June 2022; accepted 16 November 2022; published 3 January 2023)

We study acoustic topological edge modes in a honeycomb phononic crystal composed of metallic nanopillars on a LiNbO<sub>3</sub> substrate. Acoustic band calculations show that the topological surface acoustic wave (SAW) mode inhabits the edge of the honeycomb phononic crystal in spite of the hybridization with the internal acoustic modes of the substrate. Pulse-type microwave impedance microscopy realizes clear visualization of the gigahertz topological edge mode between two mutually inverted topological phononic crystals. A frequency-dependent image shows that the edge mode evolves as the bulk SAW modes are suppressed owing to the energy gap formation, consistent with the topological nature. The realization of a topological waveguide in a simple pillar structure on a substrate might pave a new path to the development of topological SAW devices for a wide range of usages such as quantum computing, sensing, and communication applications.

DOI: [10.1103/PhysRevApplied.19.014001](https://doi.org/10.1103/PhysRevApplied.19.014001)

## I. INTRODUCTION

Since the discovery of the quantum Hall effect (QHE) [1], the topological aspect of electronic states has attracted much attention [2–4]. One of the most prominent properties of topological electronic states is the formation of edge or surface states. In a two-dimensional (three-dimensional) topological crystal, for example, the edge (surface) is conducting even when the Fermi energy is located in an energy gap. The anomalous properties, including robust one-way transport along the edge (surface), are thought to be the hallmark of topological electronic states. The concept of topology is not restricted to the electronic states but is common to other Bloch states, such as photons [5], magnons [6], and phonons [7,8]. For these bosonic quantum waves, the topological edge state should work as a low dissipative waveguide, offering significant potential for applications.

Of particular importance may be the phonon, since it carries sound and heat [9]. The control of heat is one of the most important issues for resolving energy-related problems. Sound waves or higher frequency acoustic waves are also widely utilized in modern society. Among various acoustic devices, surface acoustic wave (SAW) devices have been important components for a wide range of usages [10] including quantum computing systems

[11–15] and sensing applications [16,17], as well as radio-frequency communications [18,19]. Thus, the controllability of acoustic waves contributes to their significant development. For these purposes, in the field of phononics, intensive studies have been performed for realizing various properties, such as negative refraction [20], cloaking [21], and rectification [22,23]. In particular, artificial periodic structures with a period comparable with the wavelength, termed a phononic crystal (PnC), have been developed to realize such properties. This approach can be applied to research on topological phononic properties.

Among the wide phononic spectrum ranging from kilohertz sound waves up to terahertz thermal phonons, the most prominent progress in topological research can be seen in airborne sound waves in the kilohertz range [24–29]. Since the wavelength of kilohertz sound waves is relatively long, it is possible to fabricate topological phononic crystals with centimeter-scale periodicity. Consequently, various topological acoustic phases have been quickly realized in the kilohertz region, including the Zak phase [24], the QHE [25], the quantum spin Hall effect [26], the valley Hall effect [27], the higher-order topological state [28], and Weyl semimetal states [29]. Compared with these low-frequency airborne sound waves, only a few experiments have succeeded in realizing topological acoustic states operating at much higher frequencies, such as megahertz [30–33] and gigahertz [34]. There are two reasons for this: The most critical reason is the increased difficulty of fabricating the submicron-scale device. The other reason is the high frequency

\*yoichi.nii.c1@tohoku.ac.jp

measurement with high spatial resolution. Especially for gigahertz sounds, one cannot use classical probes, such as microphones [24–29], or optical ones [30–33] because the required spatial resolution is smaller than  $1\ \mu\text{m}$ , which is below the diffraction limit of visible light. However, it seems important to realize topological acoustic properties at these high frequencies, especially in the gigahertz range, since these microwave frequencies are compatible with commercial telecommunication applications [18,19]. In addition, SAW devices with gigahertz working frequency are becoming increasingly important for the development of quantum technologies such as quantum transduction among disparate systems [12–15] and quantum control of SAWs [11]. Quite recently, with the use of microwave impedance microscopy (MIM), Zhang *et al.* observed a topological edge state of a 1 GHz acoustic wave in a two-dimensional PnC fabricated on a free-standing membrane [34]. However, the fabrication process of such a structure is cumbersome for realizing practical devices.

Here, we reveal that a patterned piezoelectric substrate hosts a similar topological waveguide of a SAW by means of acoustic band calculations and MIM. The simplified fabrication method of such a topological waveguide would be more applicable to practical devices.

## II. RESULTS AND DISCUSSION

### A. Design of a topological phononic crystal

To realize the topological edge state of acoustic waves, we fabricate periodically arranged nanopillars on a Z-cut LiNbO<sub>3</sub> substrate forming honeycomb lattices with a lattice constant  $L$  of 840 nm, as shown in Figs. 1(a) and 1(b). Their unit cell consists of two different Au cylinder-like pillars with the same height  $h = 158$  nm and substrate. The average diameter and asymmetric factor,  $\alpha = (d_m - d_n)/(d_m + d_n)$ , of the bottom diameters,  $d_m$  and  $d_n$ , for these pillars are 273 nm and 0.37, respectively. The diameters at the upper surfaces of both pillars

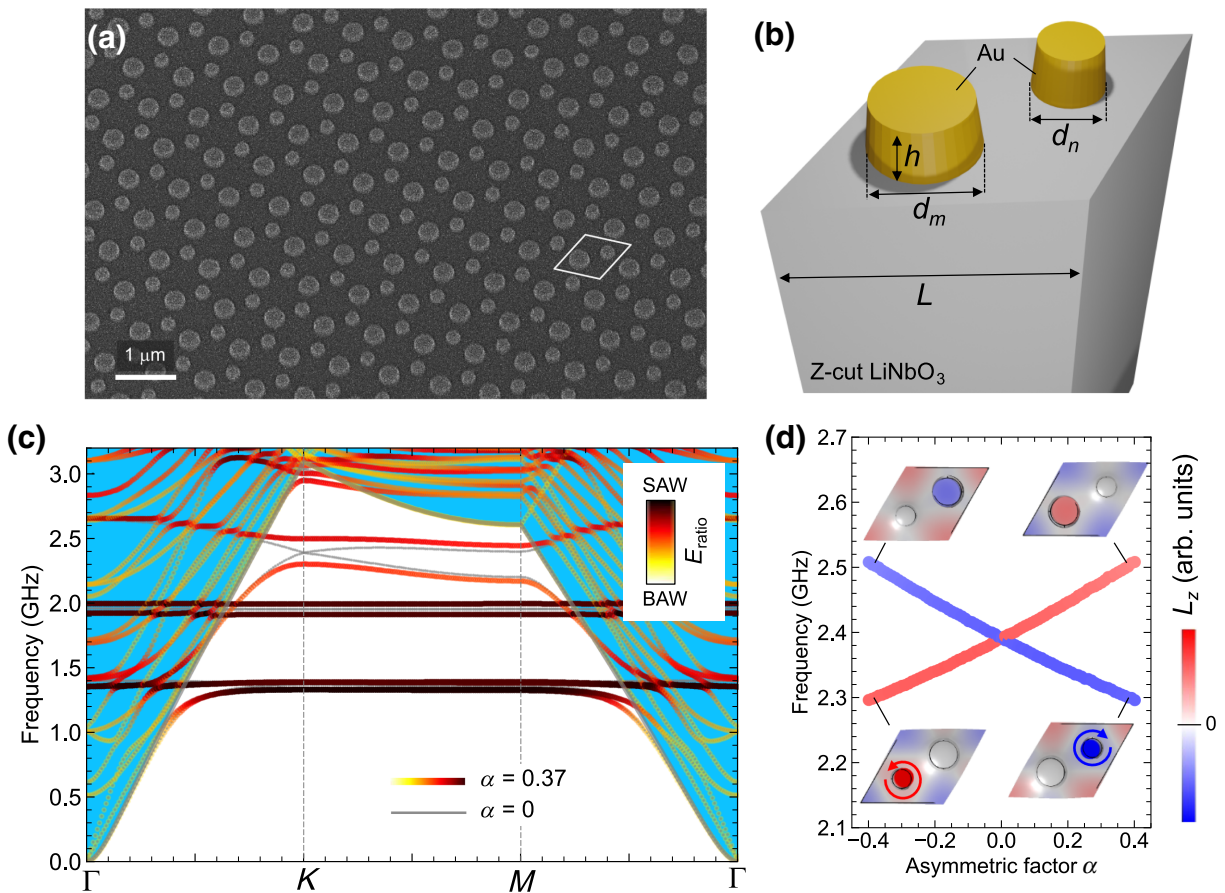


FIG. 1. (a) A scanning-electron-microscopy (SEM) image of a topological valley PnC with  $\alpha = 0.37$ . (b) A schematic diagram of the unit cell structure of the topological valley PnC in the band calculation. (c) Calculated band structure for  $\alpha = 0.37$  and  $\alpha = 0$ . For the case of  $\alpha = 0.37$ , the color represents the ratio of elastic energy in the two pillars to that of the whole unit cell including the substrate, which represents the degree of surface (bulk) nature for the eigenmode. The blue shaded region represents the area above the sound line, inhabited by bulk acoustic modes. (d) Calculated frequencies of the upper and lower SAW modes at the  $K$  point as a function of asymmetric factor  $\alpha$ . Inset represents eigenmodes of the lower and higher branches at  $\alpha = \pm 0.37$ . Red and blue colors correspond angular momentum along the  $Z$  direction.

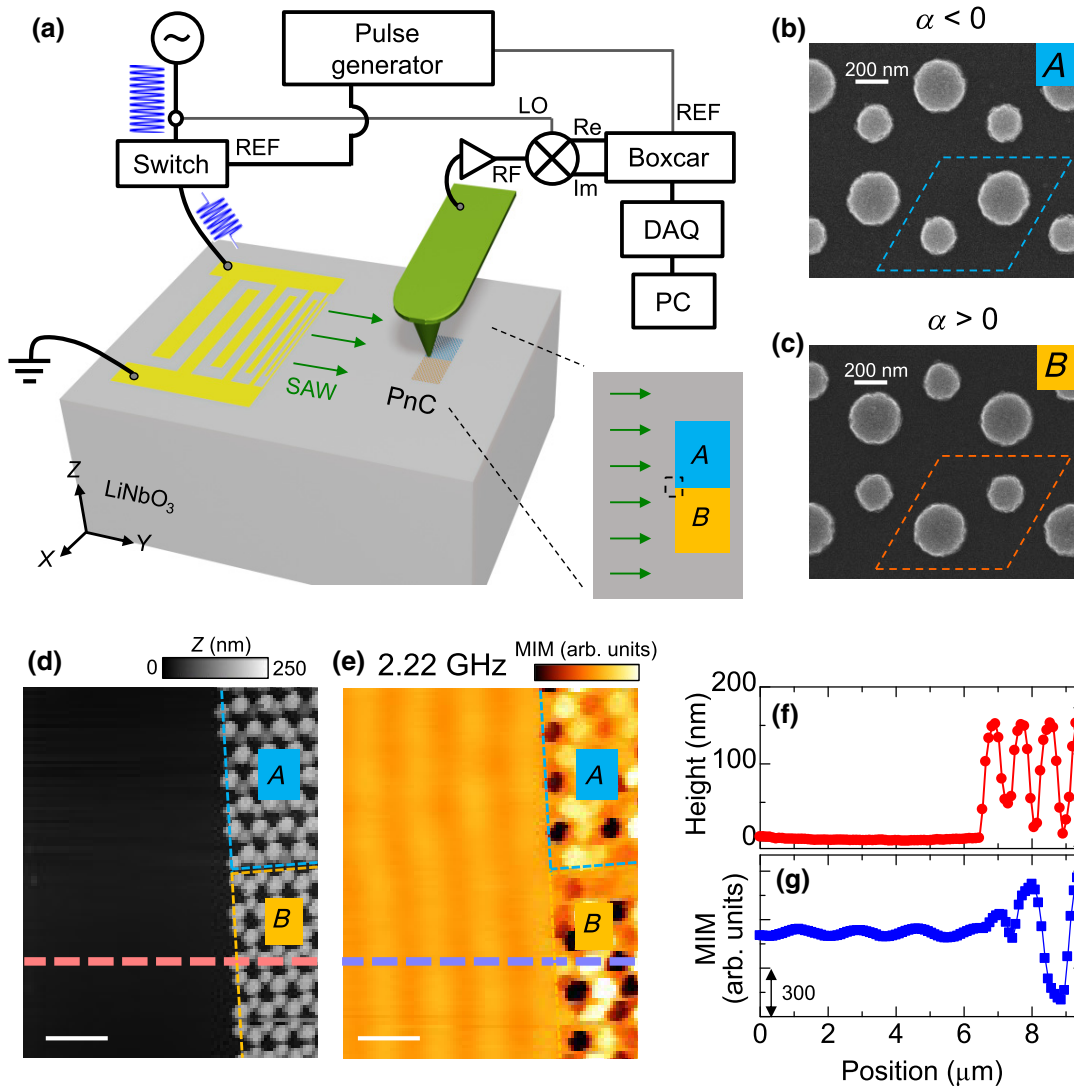


FIG. 2. (a) Setup of the MIM experiment. A chirped IDT and two mutually inverted honeycomb lattices ( $A$ ,  $B$  lattices) made of metallic pillars are fabricated on a piezoelectric substrate. By using pulse-modulated microwaves and a time-domain gating technique, only the SAW signal is detected. RF, LO, and REF stand for radio frequency, local oscillation, and reference, respectively.  $X$ ,  $Y$ , and  $Z$  axes correspond to the crystal orientation of  $\text{LiNbO}_3$ . A SAW propagates along the  $Y$  direction, which is parallel to the zigzag direction of the PnC. (b),(c) SEM images of two topological PnCs with (b)  $\alpha = -0.37$  and (c)  $\alpha = 0.37$ . (d),(e) Examples of AFM and MIM images near the  $A$ - $B$  domain boundary, as shown in the inset of (a). During scanning, a SAW with a frequency of 2.22 GHz is launched from the chirped IDT. Scale bars are  $2 \mu\text{m}$ . (f),(g) Line profiles of (f) AFM and (g) MIM images shown in the red and the blue dotted lines in (d),(e), respectively.

are 85% of those of the bottom surfaces. In electronic systems, a honeycomb lattice with two inequivalent atoms in a unit cell is known to show the quantum valley Hall effect (QVHE) [35]. In the QVHE, nontrivial Berry curvature diverges around the pair of energy extrema in momentum space, denoted as  $K$  and  $K'$  valleys. Although the total Berry curvature must be zero owing to the preserved time-reversal symmetry, its integration around each valley becomes nonzero, producing valley-dependent Chern

numbers (called valley Chern numbers). Then, topological valley transport may emerge at the interface of materials having valley Chern numbers of opposite signs. The question here is whether the SAW version of the QVHE is realized in the honeycomb-latticed pillars on a substrate. This is not so simple to answer because the internal acoustic wave mode of the substrate may be hybridized with the topological surface mode. To answer this question, we perform acoustic band calculations for the system

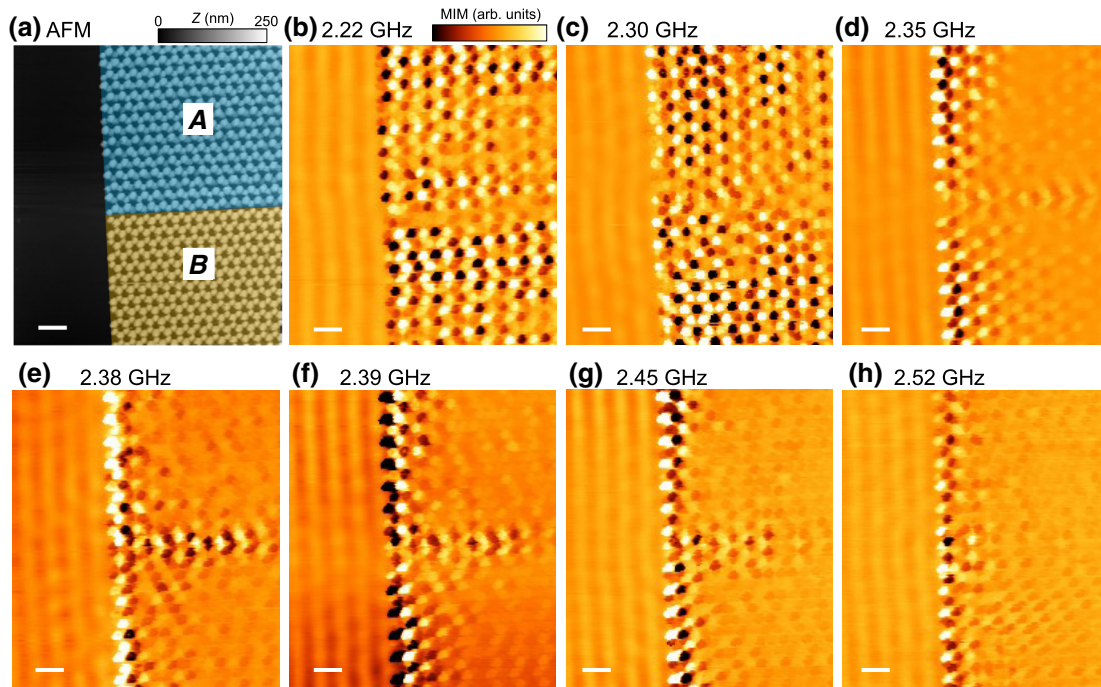


FIG. 3. (a) AFM image near the  $A$ - $B$  domain boundary. (b)–(h) MIM images at various SAW input frequencies. Scale bars are  $2 \mu\text{m}$ .

described previously [Fig. 1(b)] based on a finite-element method using commercial software COMSOL Multiphysics 5.2. To simplify the calculation, we assume that the thickness of the substrate is 4 times as large as the lattice constant of the honeycomb lattice  $L$ , while the thickness is much larger (0.5 mm) in the experiment. Details of the calculation are shown in Appendix A. Figure 1(c) shows the obtained acoustic band for  $\alpha = 0$  and  $\alpha = 0.37$ . In order to distinguish a SAW localized on the surface and a bulk acoustic wave (BAW) extending over the interior of the substrate, we evaluate for the case of  $\alpha = 0.37$  how much strain energy is concentrated on the surface. The dark red (white-to-yellow) color indicates that elastic energy is more localized at the surface (extended over the bulk), meaning that the eigenmode has a SAW (BAW) character. Because of the finite thickness of the substrate, many standing wave modes with a bulk-like nature are discerned close to the  $\Gamma$  point at finite frequencies. As the thickness increases, the number of standing wave modes increases, but all the bulk-like modes settle in the colored region irrespective of the substrate thickness. In contrast, the surface-like flat modes are discerned at around 1.4 and 2.0 GHz, originating from localized pillar resonances, as previously confirmed in various pillar-type PnCs [32,33,37]. Most important here are the dispersive surface modes around the  $K$  point. For  $\alpha = 0$ , the dispersive SAW modes show band crossing so that a Dirac point appears at the  $K$  point around 2.4 GHz. This is consistent with previous reports in the megahertz range [37]. When the asymmetry  $\alpha$  is introduced, the two-fold degeneracy at the  $K$  point is lifted,

and the SAW band gap emerges, indicating the topological valley Hall insulating state of the SAW. Importantly, these SAW modes around the  $K$  valley are well separated from the BAW modes in the colored area. Therefore, the topological nature of the two-dimensional honeycomb PnC is preserved even in the presence of the substrate. To scrutinize the topological transition, the  $\alpha$  dependences of acoustic mode frequencies at the  $K$  point are displayed in Fig. 1(d). In the course of the reversal of  $\alpha$ , the band gap at the  $K$  valley first closes and then reopens, corresponding to the reversal of valley Chern numbers. The upper and lower branches have clockwise or counterclockwise rotational strain motion. As depicted by red or blue colors in the inset of Fig. 1(d), these two rotational states are analogous to the electronic states with pseudospins of opposite sign. These acoustic band structure and resultant topological properties [35,38,39] are also reproduced by a simplified model based on the tight-binding model, in which the honeycomb-lattice nanopillars are regarded as an array of local resonators [37,40] coupled via the substrate (see Appendix B).

## B. Methods of microwave impedance microscopy and device fabrication

To directly visualize a topological SAW mode at gigahertz frequency with submicron spatial resolution, we develop a pulse-type MIM imaging system, as shown in Fig. 2(a). It is based on a commercial atomic force microscopy (AFM) system (EDU-AFM, Thorlabs)

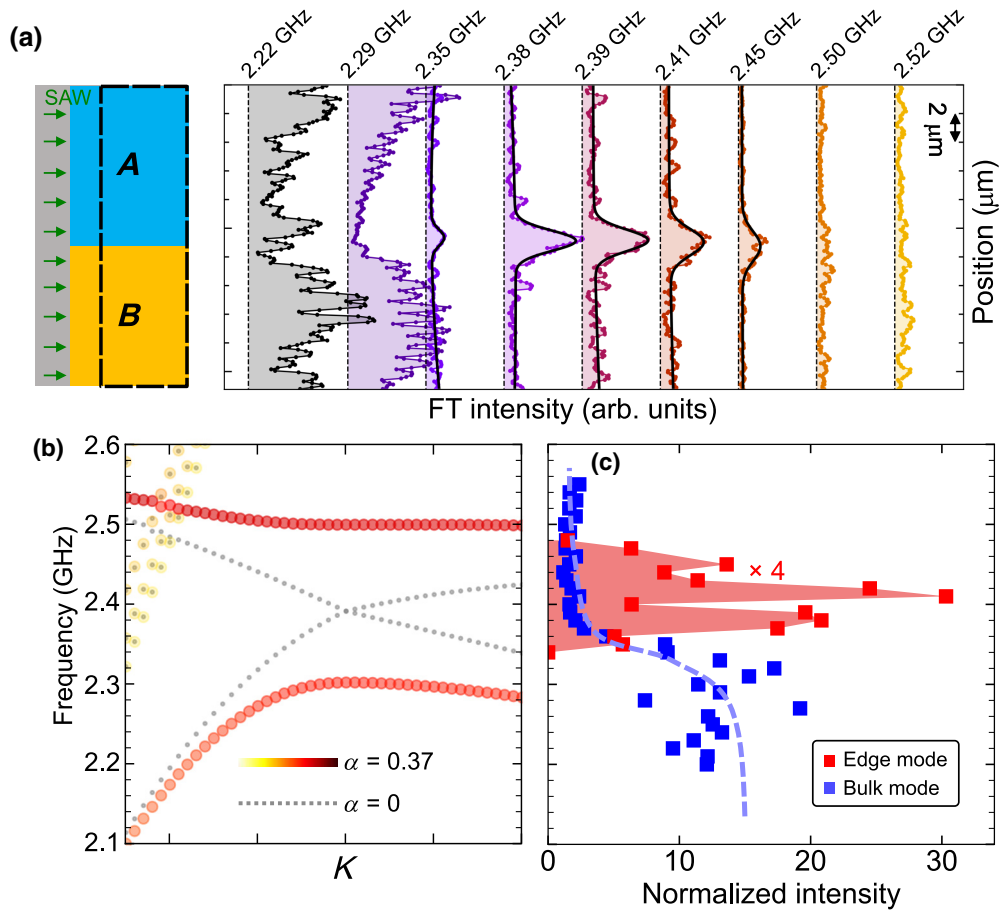


FIG. 4. (a) Vertical position dependence of SAW intensity around the  $A$ - $B$  boundary at various frequencies. The black lines between 2.35 and 2.45 GHz show the results of fitting to the Gaussian function for estimating the edge mode intensity. The dashed rectangle in the left inset represents the analyzed region for the estimation of intensity. (b) Acoustic band structure close to the SAW band gap at the  $K$  point, which is reproduced from Fig. 1(c). The color stands for the character of acoustic modes as in the Fig. 1(c). (c) Edge and bulk mode intensities as a function of the excitation frequency. These intensities were normalized by that outside the PnC. We multiply the intensities of the edge modes by a factor of 4. The blue dotted line is a guide to the eye.

and a conductive cantilever (12Pt-400B, Rocky Mountain Nanotechnology). Microwave electronics consist of a microwave generator (MG3692C, Anritsu), a pulse generator (DG645, Stanford Research Systems), an IQ mixer (MMIQ-0218LXPC, Marki Microwave), and a boxcar integrator (SR250, Stanford Research Systems). The unique feature that differentiates this from conventional MIM systems [34,41–43] is the use of pulse-modulated microwaves with a pulse duration of 150 ns. In this system, one can separate SAW and electromagnetic crosstalk in the time domain. Since the distance from the interdigital transducer (IDT) to the PnC is about 1.3 mm, SAW signals arrive at the PnC  $0.3 \mu\text{s}$  late from electromagnetic crosstalk. The time-delayed SAW signal is selectively detected by means of the boxcar integrator, and is digitized by a data acquisition (DAQ) system (NI USB-6361). An IDT and topological PnC are fabricated on a Z-cut  $\text{LiNbO}_3$  surface by using a standard electron-beam

lithography and lift-off technique. In order to excite a SAW over a wide frequency range between 2.2 and 2.55 GHz, a chirped IDT is fabricated, as schematically shown in Fig. 2(a), in which the period of the IDT is continuously varied from  $1.48$  to  $1.62 \mu\text{m}$ . The details of the fabrication process are described in the Supplemental Material [36]. To realize a topological SAW waveguide, we prepare two honeycomb lattices with valley Chern numbers of opposite signs, shown in Figs. 2(b) and 2(c), which are hereafter denoted as  $A$  and  $B$  lattices, respectively. The boundary between the upper  $A$  lattice and the lower  $B$  lattice is located at the center of the SAW propagation area, as schematically shown in the inset of Fig. 2(a). Figures 2(d) and 2(e) show typical AFM and MIM images around the  $A$ - $B$  interface. These AFM and MIM images are obtained simultaneously under SAW excitation at 2.22 GHz. On the left-hand side where there is no PnC, the periodic intensity modulation existing only in the MIM

image corresponds to the SAW launched from the left-hand IDT. This is also confirmed by the line profiles of AFM and MIM displayed in Figs. 2(f) and 2(g), respectively. The average height of the pillars measured by AFM is 153 nm, which is close to the designed total thickness of 158 nm.

### C. Imaging of the topological edge state

To demonstrate the topological SAW edge mode, we show MIM images in the vicinity of the  $A$ - $B$  interface [see Fig. 3(a)] at various frequencies between 2.22 and 2.52 GHz in Figs. 3(b)–3(h). At 2.22 and 2.30 GHz, the SAW propagating from the left-hand side readily penetrates the PnC, showing the strong contrast caused by the PnC structure. The large intensity variation in the PnC seems to have been caused by interference with the reflected SAW at the PnC boundary and the scattered SAW due to imperfections. On the other hand, at 2.52 GHz, the SAW intensity is quite suppressed in the PnC, whereas the wave front of the SAW is clearly seen before the PnC boundary. Between 2.35 and 2.45 GHz, SAW propagation is discerned only around the boundary of the  $A$ - $B$  lattices, which is the topological edge mode as discussed in the following.

To clarify the nature of the boundary mode, we examine the vertical position-dependent SAW intensity in the PnC shown in Fig. 4(a), comparing it with the band calculation around the  $K$  valley shown in Fig. 4(b). We obtain the intensity by Fourier transformation (FT) of the MIM image. The details of the FT analysis are shown in the Supplemental Material [36]. In the band calculation below 2.3 GHz, there exists a *bulk* surface acoustic mode around the  $K$  point. For this reason, we observe a large SAW intensity in the interior of the  $A$  and  $B$  lattices in this frequency range. The large and fine intensity modulations in the PnC are not attributed to measurement error, but to the vertical periodicity of the PnC and the aforementioned scattering and interference effect. This can be inferred by the fact that the intensity fluctuation outside the PnC is negligibly small, as shown in Fig. S2 (see Supplemental Material [36]). Above 2.35 GHz, the bulk surface acoustic state is gapped but the edge state should emerge according to the band calculation. This is in agreement with the experimental observation; the SAW intensity is discernible only around the interface. The edge mode intensity shows a maximum around 2.39 GHz, which seems to correspond to the Drac point for  $\alpha = 0$ . In the frequencies higher than 2.50 GHz, the upper bulk surface acoustic band shows up, but the dispersion relation is almost flat. Therefore, the SAW intensity is localized at the boundary of the PnC and suppressed inside the PnC regardless of the location. Faint contrast reflecting the PnC may originate from some residual electromagnetic crosstalk. Figure 4(c) summarizes the edge and bulk mode intensities as a function of frequency. The intensity of the edge mode is deduced from

Gaussian fitting to the position-dependent SAW intensity around the interface. The bulk mode intensity is evaluated from the FT intensity inside the PnC. Both the intensities are normalized by that outside the PnC. While the bulk mode intensity is suppressed above 2.35 GHz, the edge mode intensity rapidly increases around 2.35 GHz and shows a peak around 2.39 GHz. A small difference in the band-gap frequency between calculation and experiment may be attributable to the derivation of some material parameters used in the calculation and the fabricated PnC (see Appendix A for details). The contrastive frequency dependence of the bulk and edge intensities ensures the validity of the topological edge state.

## III. CONCLUSION

In conclusion, we demonstrate a topological SAW mode around 2.4 GHz in a honeycomb lattice made of metallic pillars on a  $\text{LiNbO}_3$  piezoelectric substrate. With the use of a pulsed MIM system, we visualize the topological edge mode. The frequency dependence of the edge mode intensity contrasts with that of the bulk SAW mode, which ensures the topological nature. While a similar topological edge state was previously realized in a purely two-dimensional system [34], the present result shows that the topological edge mode traveling along the surface is robust against hybridization with the interior BAW modes of the substrate. The method of topological patterning on a substrate seems quite useful for implementing topological waveguides and other functionalities into practical acoustic devices working at gigahertz frequencies. The achievements may contribute to the further development of SAW devices for various purposes including quantum state engineering [11], transducers [12–15], sensing [16,17], and communication applications [18,19].

## ACKNOWLEDGMENTS

We are grateful to K. Lai, D.H. Lee, and L. Zheng for the technical instruction about MIM imaging, and also grateful to T. Seki for technical advice about fabricating topological PnCs. This work is supported by JSPS KAKENHI (Grants No. JP20K03828, No. JP 21H01036, and No. JP 22H04461) and PRESTO (Grant No. JPMJPR19L6).

## APPENDIX A: NUMERICAL BAND CALCULATION

The acoustic band calculation is performed using COMSOL Multiphysics 5.2. We deduce eigenfrequencies at each specific wave vector taking the Floquet periodic boundary condition with the unit cell structure shown in Fig. 1(b). The physical parameters of the  $\text{LiNbO}_3$  substrate are density  $\rho = 4.7 \text{ g/cm}^3$ , elastic stiffness tensors  $C_{11} = 202.897$ ,  $C_{12} = 52.9177$ ,  $C_{13} = 74.9098$ ,  $C_{14} = 8.99874$ ,  $C_{33} = 243.075$ , and  $C_{44} = 59.9034 \text{ GPa}$ ,

relative permittivity coefficients  $\varepsilon_{11}=43.6$ ,  $\varepsilon_{33}=29.16$ , piezoelectric constants represented by  $e$ -form  $e_{15}=3.69594$ ,  $e_{22}=2.53764$ ,  $e_{31}=0.193644$ , and  $e_{33}=1.30863$  C/m<sup>2</sup>. The physical parameters of the Au pillars are density  $\rho=19.3$  g/cm<sup>3</sup>, Young's modulus = 79 GPa, and Poisson's ratio = 0.4. For simplicity, we do not consider the Ti layer between the Au pillars and LiNbO<sub>3</sub> substrate and instead assume that the pillars are made only of Au. We confirm that the Ti adhesion layer hardly affects the acoustic band calculation. Since LiNbO<sub>3</sub> is anisotropic, the crystal orientation of LiNbO<sub>3</sub> is prescribed as in the experiment:  $Z$  is parallel to the surface normal and  $Y$  is parallel to  $\Gamma$ - $K$  direction of the PnC.

As discussed in the main text, an eigenmode is localized on the surface (SAW-like) and another mode is extended over the interior of substrate (BAW-like). In order to identify which eigenmode is SAW-like (BAW-like), we calculate a parameter  $\eta$  of these eigenmodes given by

$$\eta = \frac{\iiint_{\text{pillars}} E(\mathbf{r})dV}{\iiint_{\text{unit cell}} E(\mathbf{r})dV},$$

where  $E(\mathbf{r})$  is the elastic energy density.  $\eta$  takes values from 0 to 1: the larger (smaller) value indicates a more SAW-like (BAW-like) character.  $\eta$  for each eigenmode of  $\alpha=0.37$  is represented by color in Fig. 1(c).

In addition, we evaluate the  $\alpha$ -dependent angular momentum at the  $K$  point. As shown in the inset of Fig. 1(d), the blue and red colors represent the angular momentum along  $Z$  direction at a position  $\mathbf{r}$ , that is evaluated by  $L_z(\mathbf{r}) = \text{Re}[u(\mathbf{r})]\text{Im}[v(\mathbf{r})] - \text{Re}[v(\mathbf{r})]\text{Im}[u(\mathbf{r})]$ , in which the  $u(\mathbf{r})$ ,  $v(\mathbf{r})$ ,  $w(\mathbf{r})$  are the  $X$ ,  $Y$ ,  $Z$  components of the complex displacement vector  $\mathbf{U}_k(\mathbf{r}, t) = (u(\mathbf{r}), v(\mathbf{r}), w(\mathbf{r}))\exp(i\omega t)$ .

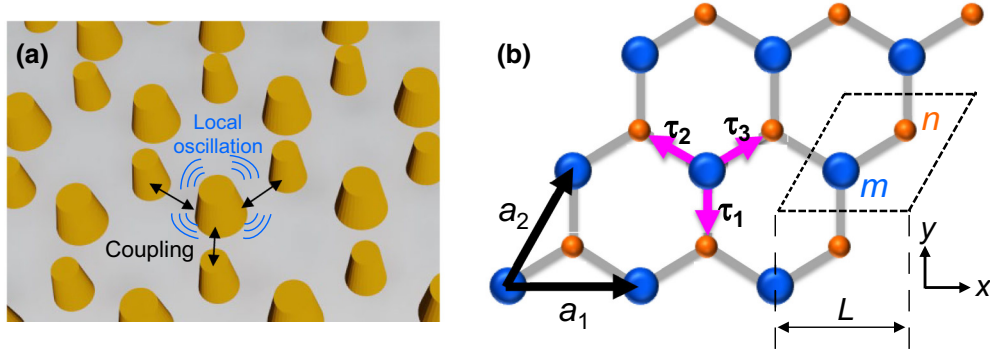


FIG. 5. (a) A schematic of honeycomb-latticed nanopillars on an elastic substrate. There are two types of pillars with distinct diameters. These are regarded as local resonators having different eigenfrequencies and are mutually coupled via the substrate. (b) A simplified model that treats the honeycomb-latticed pillars using the tight-binding approximation. Unit cell consists of two sublattices labeled by  $m$  and  $n$ , which correspond to the two pillars. The primitive translation vectors are  $\mathbf{a}_1 = L(1 \ 0)$  and  $\mathbf{a}_2 = L(1/2 \ \sqrt{3}/2)$ , and three vectors are also defined as  $\boldsymbol{\tau}_1 = L(0 \ -1/\sqrt{3})$ ,  $\boldsymbol{\tau}_2 = L(1/2 \ 1/(2\sqrt{3}))$ , and  $\boldsymbol{\tau}_3 = L(-1/2 \ 1/(2\sqrt{3}))$ . Each pillar has nearest-neighbor hopping  $t_1$  and next-nearest-neighbor hopping  $t_2$ .

## APPENDIX B: TIGHT-BINDING MODEL

To understand the topological properties of our PnC, we introduce a simplified model that is based on a discretized model. The honeycomb-latticed nanopillars can be regarded as an array of local resonators coupled via the substrate [37,40], as schematically displayed in Figs. 5(a) and 5(b). Therefore, it would be a reasonable approximation to treat it using the tight-binding framework. The tight-binding Hamiltonian of a honeycomb lattice for phononic system spanning over the  $m$  and  $n$  sublattices can be given by

$$H(\mathbf{k}) = \begin{pmatrix} \varepsilon_m + b(\mathbf{k}) & a^*(\mathbf{k}) \\ a(\mathbf{k}) & \varepsilon_n + b(\mathbf{k}) \end{pmatrix},$$

where

$$\begin{aligned} a(\mathbf{k}) &= t_1(e^{i\mathbf{k}\cdot\boldsymbol{\tau}_1} + e^{i\mathbf{k}\cdot\boldsymbol{\tau}_2} + e^{i\mathbf{k}\cdot\boldsymbol{\tau}_3}), \\ b(\mathbf{k}) &= t_2[e^{i\mathbf{k}\cdot(\boldsymbol{\tau}_2-\boldsymbol{\tau}_3)} + e^{i\mathbf{k}\cdot(\boldsymbol{\tau}_3-\boldsymbol{\tau}_1)} + e^{i\mathbf{k}\cdot(\boldsymbol{\tau}_1-\boldsymbol{\tau}_2)} + e^{i\mathbf{k}\cdot(\boldsymbol{\tau}_1-\boldsymbol{\tau}_3)} + e^{i\mathbf{k}\cdot(\boldsymbol{\tau}_2-\boldsymbol{\tau}_1)}]. \end{aligned}$$

Here  $\varepsilon_m$ ,  $\varepsilon_n$  represent on-site energies of two sublattices, and  $t_1$  and  $t_2$  are real numbers representing nearest-neighbor and next-nearest-neighbor hopping, respectively.  $\boldsymbol{\tau}_j$  ( $j=1, 2, 3$ ) indicates vectors connecting nearest-neighbor sites as shown in Fig. 5(b). Here, we assume on-site energies of the two sublattices are linearly proportional to the diameter of the nanopillars. Then, we may write them as  $\varepsilon_m = \varepsilon_0 + \alpha\Delta\varepsilon/2$  and  $\varepsilon_n = \varepsilon_0 - \alpha\Delta\varepsilon/2$ , where  $\varepsilon_0$  and  $\alpha\Delta\varepsilon$  indicate the average energy and energy

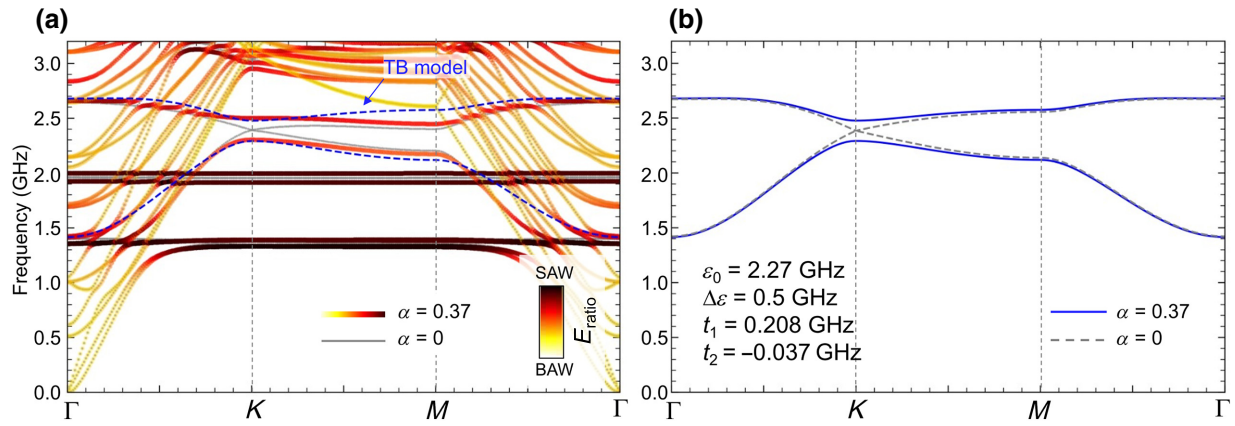


FIG. 6. Calculated acoustic band structures of  $\alpha = 0$  and  $\alpha = 0.37$  by using (a) the finite-element method and (b) the tight-binding model, respectively. The former is reproduced from Fig. 1(c). The dispersion of  $\alpha = 0.37$  deduced by the tight-binding (TB) model is also displayed in (a) for comparison. To describe (b), we use  $\varepsilon_0 = 2.27$ ,  $\Delta\varepsilon = 0.5$ ,  $t_1 = 0.208$ , and  $t_2 = -0.037$  GHz.

separation of the two sublattices, respectively. After diagonalizing the Hamiltonian, the eigenenergy can be given by

$$E(\mathbf{k}) = \varepsilon_0 + b(\mathbf{k}) \pm \sqrt{\left(\frac{\Delta\varepsilon\alpha}{2}\right)^2 + |a(\mathbf{k})|^2}.$$

The obtained dispersion relationships are shown in Fig. 6(b). The two modes start at finite frequencies at the  $\Gamma$  point and get closer to each other at the  $K$  point. This well reproduces two SAW-like modes calculated by the finite-element method as shown in Fig. 6(a).

The topological property for the honeycomb tight-binding model is well known [35,38]. To clearly demonstrate it, the momentum expansion of the Hamiltonian around  $\mathbf{K} = (4\pi/3L, 0)$  is useful. By taking up to linear order in  $\delta\mathbf{k}$ , we get

$$H(\mathbf{K} + \delta\mathbf{k}) = H_0 + H(\delta\mathbf{k}) \simeq (\varepsilon_0 - 3t_2)I + \begin{pmatrix} \Delta\varepsilon\alpha/2 & \tilde{t}\delta k_- \\ \tilde{t}\delta k_+ & -\Delta\varepsilon\alpha/2 \end{pmatrix},$$

where  $I$  indicates the  $2 \times 2$  identity matrix,  $\tilde{t} = -\sqrt{3}t_1L/2$ , and  $\delta k_{\pm} = \delta k_x \pm i\delta k_y$ . Finally, by using Pauli matrices  $\sigma_i$  ( $i = x, y, z$ ),  $H(\delta\mathbf{k})$  can be reduced to the form of the massive Dirac Hamiltonian as

$$H(\delta\mathbf{k}) = \tilde{t}(\sigma_x\delta k_x + \sigma_y\delta k_y) + M(\alpha)\sigma_z,$$

where  $M(\alpha) = \Delta\varepsilon\alpha/2$ . This is similar to the Hamiltonian describing electronic topological insulators [39]. Then, the momentum space Berry curvature for the first band is derived by [35]  $\Omega(\delta\mathbf{k}) = (1/2)\tilde{t}^2M(\alpha)[M(\alpha)^2 + \tilde{t}^2|\delta\mathbf{k}|^2]^{-3/2}$ . The integration over the  $K$  valley results in the valley Chern number, which can be given by  $C = 1/2 \text{sgn}[M(\alpha)]$  [27,38]. This obviously represents that the sign of the valley Chern number reverses with the reversal of  $M(\alpha) \propto \alpha$ .

This is consistent with the topological transition or band inversion during the reversal of  $\alpha$  as discussed in Fig. 1(d).

- 
- [1] K. v. Klitzing, G. Dorda, and M. Pepper, New Method for High-Accuracy Determination of the Fine-Structure Constant Based on Quantized Hall Resistance, *Phys. Rev. Lett.* **45**, 494 (1980).
  - [2] M. Z. Hasan and C. L. Kane, Colloquium: Topological insulators, *Rev. Mod. Phys.* **82**, 3045 (2010).
  - [3] Y. Tokura, K. Yasuda, and A. Tsukazaki, Magnetic topological insulators, *Nat. Rev. Phys.* **1**, 126 (2019).
  - [4] M. J. Gilbert, Topological electronics, *Commun. Phys.* **4**, 70 (2021).
  - [5] T. Ozawa, H. M. Price, A. Amo, N. Goldman, M. Hafezi, L. Lu, M. C. Rechtsman, D. Schuster, J. Simon, O. Zilberberg, and I. Carusotto, Topological photonics, *Rev. Mod. Phys.* **91**, 015006 (2019).
  - [6] P. A. McClarty, Topological magnons: A review, *Annu. Rev. Condens. Matter Phys.* **13**, 171 (2021).
  - [7] X. Zhang, M. Xiao, Y. Cheng, M. Lu, and J. Christensen, Topological sound, *Commun. Phys.* **1**, 97 (2018).
  - [8] Y. Liu, X. Chen, and Y. Xu, Topological phonics: From fundamental models to real materials, *Adv. Funct. Mater.* **30**, 1904784 (2019).
  - [9] M. Maldovan, Sound and heat revolutions in phononics, *Nature* **503**, 209 (2013).
  - [10] P. Delsing, A. N. Cleland, M. J. A. Schuetz, J. Knörzer, G. Giedke, J. I. Cirac, K. Srinivasan, M. Wu, C. Balram, C. Bäuerle, *et al.*, The 2019 surface acoustic waves roadmap, *J. Phys. D: Appl. Phys.* **52**, 353001 (2019).
  - [11] K. J. Satzinger, Y. P. Zhong, H.-S. Chang, G. A. Peairs, A. Bienfait, Ming-Han Chou, A. Y. Cleland, C. R. Conner, É Dumur, J. Grebel, *et al.*, Quantum control of surface acoustic-wave phonons, *Nature* **563**, 661 (2018).
  - [12] M. J. A. Schuetz, E. M. Kessler, G. Giedke, L. M. K. Vandersypen, M. D. Lukin, and J. I. Cirac, Universal Quantum Transducers Based on Surface Acoustic Waves, *Phys. Rev. X* **5**, 031031 (2015).



- [13] D. A. Golter, Th. Oo, M. Amezcua, I. Lekavicius, K. A. Stewart, and H. Wang, Coupling a Surface-Acoustic Wave to an Electron Spin in Diamond via a Dark State, *Phys. Rev. X* **6**, 041060 (2016).
- [14] O. D. D. Couto, Jr, S. Lazic, F. Iikawa, J. A. H. Stotz, U. Jahn, R. Hey, and P. V. Santos, Photon anti-bunching in acoustically pumped quantum dots, *Nat. Photonics* **3**, 645 (2009).
- [15] S. J. Whiteley, G. Wolfowicz, C. P. Anderson, A. Bourassa, H. Ma, M. Ye, G. Koolstra, K. J. Satzinger, M. V. Holt, F. J. Heremans, *et al.*, Spin-phonon interactions in silicon carbide addressed by Gaussian acoustics, *Nat. Phys.* **15**, 490 (2019).
- [16] K. Lange, B. E. Rapp, and M. Rapp, Surface acoustic wave biosensors: a review, *Anal. Bioanal. Chem.* **391**, 1509 (2008).
- [17] B. Liu, X. Chen, H. Cai, M. M. Ali, X. Tian, L. Tao, Y. Yang, and T. Ren, Surface acoustic wave devices for sensor applications, *J. Semicond.* **37**, 021001 (2016).
- [18] C. K. Campbell, *Surface Acoustic Wave Devices for Mobile and Wireless Communications* (Academic Press, San Diego, 1998).
- [19] D. Morgan, *Surface-Wave Devices for Signal Processing, Studies in Electrical and Electronic Engineering* (Elsevier, cc, 1985).
- [20] L. Feng, X. P. Liu, Y. B. Chen, Z. P. Huang, Y. W. Mao, Y. F. Chen, J. Zi, and Y. Y. Zhu, Negative refraction of acoustic waves in two-dimensional sonic crystals, *Phys. Rev. B* **72**, 033108 (2005).
- [21] S. Zhang, C. Xia, and N. Fang, Broadband Acoustic Cloak for Ultrasound Waves, *Phys. Rev. Lett.* **106**, 024301 (2011).
- [22] X. F. Li, X. Ni, L. Feng, M. H. Lu, C. He, and Y. F. Chen, Tunable Unidirectional Sound Propagation through a Sonic Crystal-Based Acoustic Diode, *Phys. Rev. Lett.* **106**, 084301 (2011).
- [23] R. Sasaki, Y. Nii, Y. Iguchi, and Y. Onose, Nonreciprocal propagation of surface acoustic wave in Ni/LiNbO<sub>3</sub>, *Phys. Rev. B* **95**, 020407(R) (2017).
- [24] M. Xiao, G. Ma, Z. Yang, P. Sheng, Z. Q. Zhang, and C. T. Chan, Geometric phase and band inversion in periodic acoustic systems, *Nat. Phys.* **11**, 240 (2015).
- [25] Y. Ding, Y. Peng, Y. Zhu, X. Fan, J. Yang, B. Liang, X. Zhu, X. Wan, and J. Cheng, Experimental Demonstration of Acoustic Chern Insulators, *Phys. Rev. Lett.* **122**, 014302 (2019).
- [26] C. He, X. Ni, H. Ge, X.-C. Sun, Y.-B. Chen, M.-H. Lu, X.-P. Liu, and Y.-F. Chen, Acoustic topological insulator and robust one-way sound transport, *Nat. Phys.* **12**, 1124 (2016).
- [27] J. Lu, C. Qui, L. Ye, X. Fan, M. Ke, F. Zhang, and Z. Liu, Observation of topological valley transport of sound in sonic crystals, *Nat. Phys.* **13**, 369 (2017).
- [28] M. Serra-Garcia, V. Peri, R. Süssstrunk, O. R. Bilal, T. Larsen, L. G. Villanueva, and S. D. Huber, Observation of a phononic quadrupole topological insulator, *Nature* **555**, 342 (2018).
- [29] F. Li, X. Huang, J. Lu, J. Ma, and Z. Liu, Weyl points and Fermi arcs in a chiral phononic crystal, *Nat. Phys.* **14**, 30 (2018).
- [30] J. Cha, K. W. Kim, and C. Daraio, Experimental realization of on-chip topological nanoelectromechanical metamaterials, *Nature* **564**, 229 (2018).
- [31] X. Xi, J. Ma, S. Wan, C. Dong, and X. Sun, Observation of chiral edge states in gapped nanomechanical graphene, *Sci. Adv.* **7**, eabe1398 (2021).
- [32] Z.-D. Zhang, S.-Y. Yu, H. Ge, J.-Q. Wang, H.-F. Wang, K.-F. Liu, T. Wu, C. He, M.-H. Lu, and Y.-F. Chen, Topological Surface Acoustic Waves, *Phys. Rev. Appl.* **16**, 044008 (2021).
- [33] J.-Q. Wang, Z.-D. Zhang, S.-Y. Yu, H. Ge, K.-F. Liu, T. Wu, X.-C. Sun, L. Liu, H.-Y. Chen, C. He, *et al.*, Extended topological valley-locked surface acoustic waves, *Nat. Commun.* **13**, 1324 (2022).
- [34] Q. Zhang, D. Lee, L. Zheng, X. Ma, S. I. Meyer, L. He, H. Ye, Z. Gong, B. Zhen, K. Lai, *et al.*, Gigahertz topological valley Hall effect in nanoelectromechanical phononic crystals, *Nat. Electron.* **5**, 157 (2022).
- [35] D. Xiao, W. Yao, and Q. Niu, Valley-Contrasting Physics in Graphene: Magnetic Moment and Topological Transport, *Phys. Rev. Lett.* **99**, 236809 (2007).
- [36] See Supplemental Material at <http://link.aps.org/supplemental/10.1103/PhysRevApplied.19.014001> for details of device fabrication and MIM analysis.
- [37] S.-Y. Yu, X.-C. Sun, X. Ni, Q. Wang, X.-J. Yan, C. He, X.-P. Liu, L. Feng, M.-H. Lu, and Y.-F. Chen, Surface phononic graphene, *Nat. Mater.* **15**, 1243 (2016).
- [38] F. Zhang, A. H. MacDonald, and E. J. Mele, Valley Chern numbers and boundary modes in gapped bilayer graphene, *Proc. Natl. Acad. Sci. U. S. A.* **110**, 10546 (2013).
- [39] B. A. Bernevig, T. L. Hughes, and S.-C. Zhang, Quantum spin Hall effect and topological phase transition in HgTe quantum wells, *Science* **314**, 1757 (2006).
- [40] R. K. Pal and M. Ruzzene, Edge waves in plates with resonators: an elastic analogue of the quantum valley Hall effect, *New J. Phys.* **19**, 205001 (2017).
- [41] K. Lai, W. Kundhikanjana, M. Kelly, and Z. X. Shen, Modeling and characterization of a cantilever-based near-field scanning microwave impedance microscope, *Rev. Sci. Instrum.* **79**, 063703 (2008).
- [42] L. Zheng, D. Wu, X. Wu, and K. Lai, Visualization of Surface-Acoustic-Wave Potential by Transmission-Mode Microwave Impedance Microscopy, *Phys. Rev. Appl.* **9**, 061002(R) (2018).
- [43] L. Zheng, L. Shao, M. Loncar, and K. Lai, Imaging acoustic waves by microwave microscopy: microwave impedance microscopy for visualizing gigahertz acoustic waves, *IEEE Microwave Mag.* **21**, 60 (2020).